COMMUNICATION

Check for updates

Pressure regulated CO_2 electrolysis on two-dimensional Bi_2O_2Se†

Ruofan Sun,‡ Jiwu Zhao,‡ Hang Liu, [ID] Yanrong Xue and Xu Lu [ID] *

The electrochemical reduction of carbon dioxide (CO_2RR) offers potential for sustainable production and greenhouse gas mitigation, particularly with renewable energy integration. However, its widespread application is hindered by expensive catalysts, low selectivity, and limited current density. This study addresses these challenges by developing a low-mass-loading two-dimensional (2D) Bi_2O_2Se catalyst *via* chemical vapor deposition (CVD). The catalyst achieves a formate faradaic efficiency (FE) of 47.1% with a high current density of 4649 mA mg^{-1} at −1.15 V (*vs.* RHE), significantly outperforming bulk Bi_2O_2Se. Pressurizing CO_2, a condition commonly encountered in industrial processes, further enhances formate selectivity and current density, increasing from 2189 mA mg^{-1} at ambient pressure (1.01 bar) to 7457 mA mg^{-1} at 40 bar. *In situ* Raman spectroscopy and DFT calculations reveal the intermediates and pathways involved, underscoring the critical role of pressure in regulating CO_2RR pathways. These findings highlight the potential of 2D catalysts for sustainable and industrially relevant CO_2 conversion under high pressure.

Production of value-added chemicals *via* renewable-driven electrochemical reduction of CO_2 (CO_2RR) holds promise to deal with the pressing global warming and energy crisis.[1–3] To date, the predominant focus of CO_2RR research lies in examining its performance under ambient pressure conditions, while industrial CO_2 is typically pressurized during capture, transport, and storage. Coincidentally, CO_2RR benefits from high pressure in aqueous solutions because low CO_2 solubility under ambient pressure usually leads to the formation of unfavorable active carbon species, and subsequently causes diminished current density and reduced selectivity.[4–6] We have reported that higher CO_2 pressure can significantly improve the formate selectivity during aqueous-based CO_2RR over commonly used catalysts

such as Cu, Au, Ag and Sn.[7] Cu_2O@Cu catalysts with a hollow sphere morphology were also found to produce ethanol when operating under pressure.[8] These studies pointed out the important role of high pressure in regulating the CO_2RR pathways.

Bismuth-based catalysts have garnered considerable interest in the CO_2RR field because of their high selectivity toward formate, cost effectiveness and low toxicity, rendering them a capable material for large-scale applications.[3,9] Two-dimensional (2D) bismuth materials have aroused increasing attention in light of their high specific surface area, large atomic exposure rate and tunable electronic states.[10] Han *et al.* showcased the effectiveness of ultrathin BiNS catalysts, achieving superior formate selectivity (>90% FE), current density (24 mA cm^{-2}), and durability.[11] Peng *et al.* synthesized ultrathin bismuth nanosheets (1.02 nm thick) with enhanced intrinsic activity and abundant active sites.[12,13] Recently, 2D Bi_2O_2Se has emerged as a robust semiconducting material with ultra-high electron mobility and quantum oscillations,[14] and we believe that 2D Bi_2O_2Se may hold the potential to catalyze the CO_2RR effectively. Moreover, 2D Bi_2O_2Se may be highly cost-effective: on the one hand, Bi is a kind of non-noble metal and on the other hand, 2D materials exhibit low mass loading.

Here we report the pressure-regulated CO_2RR to formate as catalyzed by 2D Bi_2O_2Se. The 2D Bi_2O_2Se catalyst with a layered "2D Zipper" structure is synthesized by a chemical vapor deposition (CVD) method on glassy carbon. While the catalyst loading is as low as 5.2 μg cm^{-2}, our 2D Bi_2O_2Se manifests a CO_2RR current density as high as 4649 mA mg^{-1} with a formate FE of 47%, surpassing reported Bi based 2D catalysts and the Bi_2O_2Se bulk counterparts. By pressurizing CO_2 from ambient pressure (1.01 bar) to 40 bar, we steer the CO_2RR pathway toward formate, achieving a record-high current density of 7084 mA mg^{-1} with a formate FE of 78%. *In situ* Raman spectroscopy and density functional theory (DFT) calculations reveal the mechanism of CO_2RR to formate under high pressure, evidencing a stronger CO_2 adsorption, enhanced *OCHO intermediate formation and more favorable pathway.

Division of Physical Science and Engineering (PSE), King Abdullah University of Science and Technology (KAUST), Thuwal, 23955-6900, Kingdom of Saudi Arabia
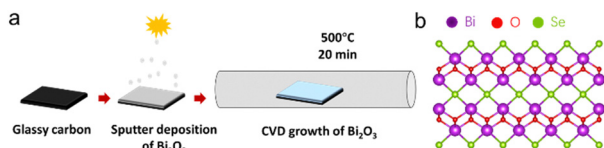† Electronic supplementary information (ESI) available. See DOI: https://doi.org/10.1039/d4cc05357e
‡ These authors contributed equally.

Fig. 1 Schematic of (a) 2D Bi_2O_2Se synthesis by CVD and (b) the atomic structure.

Fig. 2 Effective utilization of the 2D catalyst. (a) CO_2RR to $HCOO^-$ performance of 2D Bi_2O_2Se and Bi_2O_2Se bulk at 1.01 bar. (b) The comparison of some typical Bi-based 2D catalysts for CO_2RR to $HCOO^-$ with 2D Bi_2O_2Se.

The 2D Bi_2O_2Se was synthesized through a two-step process: (i) preparation of bismuth oxide on glassy carbon *via* E-beam evaporation and (ii) selenization by the CVD method (Fig. 1a). Using glassy carbon as the substrate allowed the *in situ* synthesis of 2D Bi_2O_2Se, enabling its direct use as a working electrode in H-cell setups without the need for 2D material transfer. Fig. 1b illustrates the atomic structure of Bi_2O_2Se, which comprises alternating layers of bismuth atoms in hexagonal lattices, oxygen atoms positioned between these layers, and selenium atoms filling the interlayer gaps.[15] As documented in the literature, the Raman peak at the A_{1g} mode (159 cm^{-1}) indicates the symmetric stretching vibration mode of the Bi–O bonds in the Bi_2O_2 layer (Fig. S1, ESI†).[16] The lattice structure of Bi_2O_2Se was confirmed using high-angle annular dark-field scanning transmission electron microscopy (HAADF-STEM), which aligns with the proposed "2D Zipper" model (Fig. S2, ESI†).[17] This model suggests that the chemical bonds near the surface of Bi_2O_2Se are strengthened, enhancing the stability of the few-layer structures. Additionally, electron energy loss spectroscopy (EELS) mapping of Bi_2O_2Se revealed a uniform distribution of Bi, O, and Se elements across the entire area (Fig. S3, ESI†). Atomic force microscopy (AFM) characterization on Bi_2O_2Se confirmed an average thickness of 10.49 nm (Fig. S4, ESI†), revealing 17 layers of 2D monolayer.[14] This thickness suggests a low catalyst mass loading, which was further validated by inductively coupled plasma mass spectrometry (ICP-MS), revealing a catalyst loading of 5.2 µg cm^{-2}. X-ray photoelectron spectroscopy (XPS) was used to verify the presence of Bi, O, and Se (Fig. S5 and S6, ESI†). The spectra revealed two oxidation states of the Bi atom, represented by Bi $4f_{7/2}$ and Bi $4f_{5/2}$ at binding energies of 159 and 164 eV, respectively, as well as O 1s states at 530 eV and Se 3d states at 53 eV, consistent with previous reports.[18] These observations authenticated the successful synthesis of 2D Bi_2O_2Se and motivated us to conduct the subsequent electrochemical experiments.

In contrast to wet chemical reduction,[19] galvanic replacement reaction,[20] hydrothermal reaction,[21] and electrochemical conversion[22] methods, the direct CVD growth of 2D Bi-based catalysts on glassy carbon substrates offers low mass loading by depositing only a few layers of catalyst (Fig. S4, ESI†). This may also enhance electron transport from the conductive substrate to the 2D catalyst. The CO_2RR activity of 2D Bi_2O_2Se was firstly assessed in 0.5 M $KHCO_3$ electrolyte by linear sweep voltammetry (LSV) at ambient pressure (1.01 bar), as shown in Fig. S7 (ESI†). In a CO_2 saturated electrolyte, the 2D Bi_2O_2Se demonstrates a higher current density compared to an N_2 saturated electrolyte at -0.7 V *vs.* reversible hydrogen electrode (RHE),
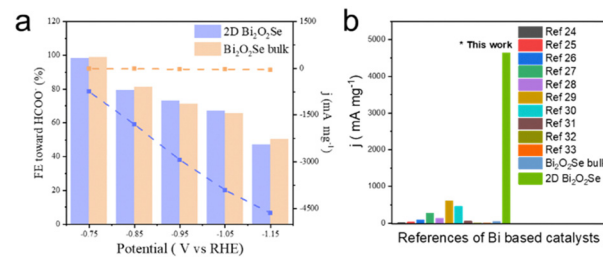
indicating a greater favorability for CO_2RR over the hydrogen evolution reaction (HER).

To assess the activity in terms of current density per unit mass (mA mg^{-1}) and faradaic efficiency (FE), we compared the synthesized 2D Bi_2O_2Se with Bi_2O_2Se bulk prepared by the spin coating method with catalyst loading of 0.5 mg cm^{-2} (Fig. 2a). As shown in Fig. S8 (ESI†), 1H nuclear magnetic resonance (NMR) analysis identified formate as the only liquid product from the CO_2RR, while gas chromatography (GC) detected H_2 and CH_4 as the gas products. It was observed that 2D Bi_2O_2Se exhibits significantly higher current density per unit mass, reaching 4649 mA mg^{-1} at -1.15 V (*vs.* RHE), which is 2 orders of magnitude greater than that of the bulk counterpart. However, the FE toward formate for both 2D Bi_2O_2Se and Bi_2O_2Se bulk remained at the same level and decreased with increased potential. This was attributed to the stronger dependence of the Volmer step potential on the overall potential compared to CO_2 adsorption, leading to a higher preference for the HER at more negative potentials (Fig. S8, ESI†).[23] To understand the specific surface area properties of 2D Bi_2O_2Se and Bi_2O_2Se bulk, electrochemically active surface area (ECSA) calculation (Fig. S9 and S10, ESI†) and non-mass-normalized LSV (Fig. S7, ESI†) were performed. Both 2D Bi_2O_2Se and Bi_2O_2Se bulk exhibit similar surface area and non-mass-normalized current density, indicating minimal effect of ECSA when comparing the mass-normalized CO_2RR current density. More than that, we found that both Bi_2O_2Se and Bi_2O_3 were firstly reduced to the Bi metal state and it is Bi (012) that acts as the main facet during the CO_2RR (Fig. S11, ESI†). These findings suggested that 2D Bi_2O_2Se growth on glassy carbon enabled more effective utilization of the catalyst in light of the low mass loading, while maintaining comparable CO_2RR activity compared to bulk Bi_2O_2Se. A similar trend can be found when comparing 2D Bi_2O_3 and Bi_2O_3Se bulk (Fig. S12, ESI†). Furthermore, the CVD grown 2D Bi_2O_2Se catalyst greatly outperforms the benchmarks in the literature, including mesoporous Bi nanosheets,[24] freestanding 2D bismuth nanosheets,[25] layered Bi nanosheets,[26] electron-rich Bi nanosheets,[27] 3D network of interconnected 2D bismuthene arrays,[28] atomically thin bismuthene with rich defects,[29] heterostructured bismuth-based catalysts,[30] $Bi_2O_2CO_3$ nanosheets[31] and Bi-MOF[32,33] (Fig. 2b).

Pressurization of CO_2 has been reported to steer the selectivity[34,35] and boost the CO_2RR current density.[4,36] To further
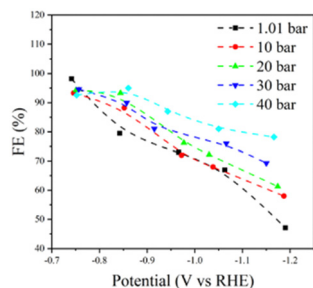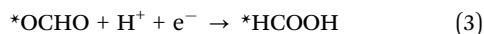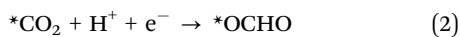
Fig. 3 Partial current density of pressure regulated CO_2RR to formate on 2D Bi_2O_2Se.
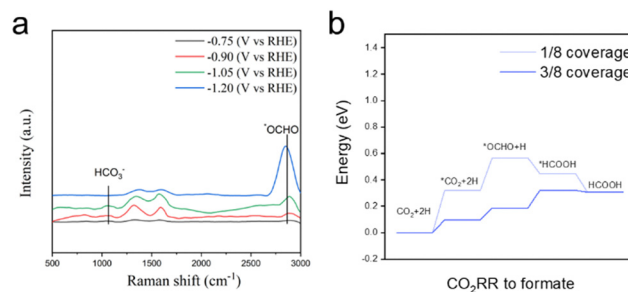

Fig. 4 Mechanism study on high pressure CO_2RR to formate over 2D Bi_2O_2Se. (a) *In situ* Raman spectroscopy measurements at 20 bar. (b) Free energy diagram of adsorbed CO_2RR intermediates with the CO_2 coverages of 1/8 ML and 3/8 ML.

enhance the CO_2RR performance of our 2D Bi_2O_2Se catalyst, we subjected the system to elevated CO_2 pressures ranging from 1.01 to 40 bar. In general, the FE towards formate increased as the CO_2 pressure increased, rising from 79.5% at 1.01 bar to 95% at 40 bar at -0.85 V (*vs.* RHE) (Fig. S13, ESI†). This demonstrates the capability of pressurized CO_2 to regulate the selectivity towards formate on 2D Bi_2O_2Se, consistent with previous study.[7] The corresponding total and formate partial current densities at various CO_2 pressures are plotted in Fig. S14 (ESI†) and Fig. 3. In particular, the formate partial current density was improved from 2146 to 7308 mA mg^{-1} when the pressure increased from 1.01 to 40 bar at -1.15 V, indicating a greatly promoted production rate of formate. To compare the 2D Bi_2O_2Se with Bi_2O_2Se bulk under high CO_2 pressure, we plotted current densities with corresponding formate FEs (Fig. 2a and Fig. S15, ESI†). The results align with prior research, underscoring the efficacy of our 2D Bi_2O_2Se catalyst with minimal mass loading in sustaining high current densities. As depicted in Fig. S16 (ESI†), Nyquist plots for CO_2RR over the 2D Bi_2O_2Se catalyst showed a decrease in charge transfer resistance with increased CO_2 pressures. This indicates that a significantly accelerated electron transfer with higher CO_2 pressure as enhanced CO_2 solubility in electrolytes promoted reactant transportation to the electrodes, that means, despite HER being more favorable under more negative potentials according to previous reported works,[37,38] the elevated CO_2 pressure can still suppress the HER (Fig. S8 and S17, ESI†).

These findings motivated us to investigate the mechanism of the CO_2RR to formate under high CO_2. In general, the CO_2RR to formate pathway follows 4 steps:

$$CO_2 + * \rightarrow *CO_2 \qquad (1)$$

$$*CO_2 + H^+ + e^- \rightarrow *OCHO \qquad (2)$$

$$*OCHO + H^+ + e^- \rightarrow *HCOOH \qquad (3)$$

$$*HCOOH \rightarrow * + HCOOH \qquad (4)$$

In order to track reaction intermediates during CO_2RR over 2D Bi_2O_2Se, *in situ* Raman spectroscopy measurements were performed in ambient CO_2 pressure (1.01 bar) and pressurized CO_2 (20 bar) (Fig. 4a and Fig. S18, ESI†). In the scan of applied potential from -0.75 to -1.2 V *vs.* RHE over the 2D Bi_2O_2Se catalyst, two intrinsic Raman peaks were detected. The Raman peaks at 1052 cm^{-1} were attributed to HCO_3^-, respectively,

indicating a CO_2 saturated environment during the CO_2RR.[39,40] In addition, the peak at 2898 cm^{-1} was ascribed to the C–H stretching of *OCHO radicals.[41] This revealed the favored *CO_2^- formation to activate CO_2 molecules and enhanced adsorption strength of *OCHO intermediates, leading to superior activity and selectivity toward formate. Due to the low catalyst loading and strong Raman signal from glassy carbon, the D band and G band of glassy carbon were observed at 1346 cm^{-1} and 1572 cm^{-1}. To gain a deep understanding on high pressure CO_2RR, the DFT and *Ab initio* molecular dynamic (AIMD) calculations were performed in the Vienna Ab initio Simulation Package (VASP). In light of the pressure dependent CO_2 solubility, we sought to explore the influence of CO_2 coverage from 1/8 monolayer (ML) to 3/8 ML on the Bi (012) facet, the dominant facet of the prepared catalyst, confirmed by X-ray diffraction (XRD) measurement, as shown in Fig. S11 (ESI†).

The optimized structures and free energy diagram of adsorbed CO_2RR to formate intermediates are depicted in Fig. S19 (ESI†) and Fig. 4b. In the initial step ($CO_2 + * \rightarrow$ *CO_2), a smaller free energy difference for 3/8 ML CO_2 coverage (0.1 eV) indicated a stronger CO_2 adsorption when compared with that of 1/8 ML CO_2 coverage (0.32 eV). The first proton-coupled electron transfer process (*CO_2 + H$^+$ + e$^-$ $\rightarrow$ *OCHO) was defined as the rate-determine-step (RDS) of the CO_2RR to formate with 1/8 ML CO_2 coverage due to the large uphill energy. Moreover, in this step, the required free energy for 3/8 ML coverage is 0.1 eV, notably lower than that for 1/8 ML coverage (0.25 eV). That is, CO_2RR under high pressure exhibits higher activity for *OCHO formation due to the lower reaction energy barrier. For the CO_2RR to formate with 3/8 ML CO_2 coverage, the second proton-coupled electron transfer process (*OCHO + H$^+$ + e$^-$ $\rightarrow$ *HCOOH) was defined as the RDS. This proton-coupled electron transfer process (*OCHO + H$^+$ + e$^-$ $\rightarrow$ *HCOOH) and the desorption process (*HCOOH $\rightarrow$ * + HCOOH) contributed to the final formate production. The free energy difference of these two steps with 3/8 ML CO_2 coverage is lower, revealing a more favorable pathway. DFT calculations on the HER under pressurized CO_2 were also conducted, as shown in Fig. S20 (ESI†). HER exhibited decreased energy barrier for RDS from 1 V to 0.92 V with enhanced CO_2 coverage from 1/8 ML to 3/8 ML, whereas the CO_2RR has an RDS energy barrier of

only 0.13 V under high pressure. As a result, CO_2RR is preferred compared to HER as the pressure increases, aligning with the experimental data (Fig. S8 and S17, ESI†).

In conclusion, we devise a low-mass-loading 2D Bi_2O_2Se catalyst and leverage the pressure to enhance CO_2RR for formate production. The 2D catalyst exhibited a significantly higher current density of 4649 mA mg^{-1} with 47.1% FE to formate at −1.15 V (vs. RHE) compared to the bulk phase, indicating its cost-effectiveness. High CO_2 pressure, commonly encountered in industrial processes involving CO_2 capture, transport, and storage, significantly enhances formate selectivity and current density during CO_2RR. Under high pressure, the partial current density increases from 2146 mA mg^{-1} at 1.01 bar to 7308 mA mg^{-1} at 40 bar at −1.15 V. Moreover, in situ Raman measurements and DFT calculations under pressurized CO_2RR revealed the intermediates and pathways involved. These findings highlight the potential of 2D catalysts for sustainable CO_2 conversion at high pressure with industrial relevance and underscore the importance of pressure in regulating the CO_2RR pathways.

Data availability

The data supporting the findings of this study are available within the article and its ESI.† Additional raw data and experimental details can be provided by the corresponding author upon reasonable request.

Conflicts of interest

There are no conflicts to declare.

Notes and references

1 O. S. Bushuyev, P. De Luna, C. T. Dinh, L. Tao, G. Saur, J. van de Lagemaat, S. O. Kelley and E. H. Sargent, Joule, 2018, 2, 825–832.
2 S. Yoshida, M. Sampei, N. Todoroki, E. Hisamura, K. Nakao, K. Albrecht and T. Wadayama, Chem. Commun., 2023, 59, 3459–3462.
3 B.-Q. Miao, W.-S. Fang, B. Sun, F.-M. Li, X.-C. Wang, B.-Y. Xia and Y. Chen, Chin. J. Struct. Chem., 2023, 42, 100095.
4 J. Li, Y. Kuang, Y. Meng, X. Tian, W.-H. Hung, X. Zhang, A. Li, M. Xu, W. Zhou and C.-S. Ku, J. Am. Chem. Soc., 2020, 142, 7276–7282.
5 J. Li, J. Guo and H. Dai, Sci. Adv., 2022, 8, eabo0399.
6 S. Ruan, B. Zhang, J. Zou, W. Zhong, X. He, J. Lu, Q. Zhang, Y. Wang and S. Xie, Chin. J. Catal., 2022, 43, 3161–3169.
7 L. Huang, G. Gao, C. Yang, X.-Y. Li, R. K. Miao, Y. Xue, K. Xie, P. Ou, C. T. Yavuz and Y. Han, Nat. Commun., 2023, 14, 2958.
8 R. Qiu, J. Jia, L. Peng, R. Li, S. Yan, J. Li, J. Zhang, D. T. Sun, Z. Lan and T. Xue, Green Chem., 2023, 25, 684–691.
9 B. Ávila-Bolívar, V. Montiel and J. Solla-Gullón, ChemElectroChem, 2022, 9, e202200272.
10 S. Lu, F. Lou and Z. Yu, Catalysts, 2022, 12, 228.
11 N. Han, Y. Wang, H. Yang, J. Deng, J. Wu, Y. Li and Y. Li, Nat. Commun., 2018, 9, 1320.
12 C. J. Peng, X. T. Wu, G. Zeng and Q. L. Zhu, Chem. – Asian J., 2021, 16, 1539–1544.
13 S. Liu, Y. Fan, Y. Wang, S. Jin, M. Hou, W. Zeng, K. Li, T. Jiang, L. Qin and Z. Yan, Nano Lett., 2022, 22, 9107–9114.
14 J. Wu, H. Yuan, M. Meng, C. Chen, Y. Sun, Z. Chen, W. Dang, C. Tan, Y. Liu and J. Yin, Nat. Nanotechnol., 2017, 12, 530–534.
15 H. Zhou, X. Zhu, W. Liu, S. Liu, Y. Ding, Q. Zhang, Z. Zhang and R. Zhang, Appl. Surf. Sci., 2024, 672, 160851.
16 W. Chen, U. Khan, S. Feng, B. Ding, X. Xu and B. Liu, Adv. Funct. Mater., 2020, 30, 2004960.
17 Q. Wei, R. Li, C. Lin, A. Han, A. Nie, Y. Li, L.-J. Li, Y. Cheng and W. Huang, ACS Nano, 2019, 13, 13439–13444.
18 M. T. Hossain and P. Giri, J. Appl. Phys., 2021, 129, 17.
19 H. Xie, T. Zhang, R. Xie, Z. Hou, X. Ji, Y. Pang, S. Chen, M. M. Titirici, H. Weng and G. Chai, Adv. Mater., 2021, 33, 2008373.
20 J. Fan, X. Zhao, X. Mao, J. Xu, N. Han, H. Yang, B. Pan, Y. Li, L. Wang and Y. Li, Adv. Mater., 2021, 33, 2100910.
21 J. Ma, J. Yan, J. Xu, J. Ni, R. Li, L. Li and L. Lu, Chem. – Eur. J., 2022, 28, e202201747.
22 P. Liu, H. Liu, S. Zhang, J. Wang and C. Wang, J. Colloid Interface Sci., 2021, 602, 740–747.
23 P. D. Pedersen, M. M. Melander, T. Bligaard, T. Vegge, K. Honkala and H. A. Hansen, J. Phys. Chem. C, 2023, 127, 18855–18864.
24 H. Yang, N. Han, J. Deng, J. Wu, Y. Wang, Y. Hu, P. Ding, Y. Li, Y. Li and J. Lu, Adv. Energy Mater., 2018, 8, 1801536.
25 F. Yang, A. O. Elnabawy, R. Schimmenti, P. Song, J. Wang, Z. Peng, S. Yao, R. Deng, S. Song and Y. Lin, Nat. Commun., 2020, 11, 1088.
26 Y. Qiao, W. Lai, K. Huang, T. Yu, Q. Wang, L. Gao, Z. Yang, Z. Ma, T. Sun and M. Liu, ACS Catal., 2022, 12, 2357–2364.
27 Z. Li, B. Sun, D. Xiao, Z. Wang, Y. Liu, Z. Zheng, P. Wang, Y. Dai, H. Cheng and B. Huang, Angew. Chem., Int. Ed., 2023, 62, e202217569.
28 Y. C. He, D. D. Ma, S. H. Zhou, M. Zhang, J. J. Tian and Q. L. Zhu, Small, 2022, 18, 2105246.
29 M. Zhang, W. Wei, S. Zhou, D.-D. Ma, A. Cao, X.-T. Wu and Q.-L. Zhu, Energy Environ. Sci., 2021, 14, 4998–5008.
30 P. F. Sui, C. Xu, M. N. Zhu, S. Liu, Q. Liu and J. L. Luo, Small, 2022, 18, 2105682.
31 T. Fan, W. Ma, M. Xie, H. Liu, J. Zhang, S. Yang, P. Huang, Y. Dong, Z. Chen and X. Yi, Cell Rep. Phys. Sci., 2021, 2, 3.
32 Z. W. Yang, J. M. Chen, Z. L. Liang, W. J. Xie, B. Zhao and L. N. He, ChemCatChem, 2023, 15, e202201321.
33 Q. Huang, X. Sha, R. Yang, H. Li and J. Peng, ACS Appl. Mater. Interfaces, 2024, 16, 13882–13892.
34 C. M. Gabardo, A. Seifitokaldani, J. P. Edwards, C.-T. Dinh, T. Burdyny, M. G. Kibria, C. P. O'Brien, E. H. Sargent and D. Sinton, Energy Environ. Sci., 2018, 11, 2531–2539.
35 K. Hara, A. Kudo and T. Sakata, J. Electroanal. Chem., 1995, 391, 141–147.
36 E. J. Dufek, T. E. Lister, S. G. Stone and M. E. McIlwain, J. Electrochem. Soc., 2012, 159, F514.
37 X.-Z. Wang, S. Liu, Q. Liu and J.-L. Luo, Electrochem. Commun., 2019, 107, 106531.
38 R. Sun, J. Zhao and X. Lu, J. Mater. Chem. A, 2024, 12, 8429–8437.
39 A. Dutta, I. n Zelocualtecatl Montiel, K. Kiran, A. Rieder, V. Grozovski, L. Gut and P. Broekmann, ACS Catal., 2021, 11, 4988–5003.
40 H. Li, P. Wei, D. Gao and G. Wang, Curr. Opin. Green Sustainable Chem., 2022, 34, 100589.
41 S. Jiang, K. Klingan, C. Pasquini and H. Dau, J. Chem. Phys., 2019, 150, 4.